Applied Surface Science 628 (2023) 157145

Contents lists available at ScienceDirect

Applied Surface Science

journal homepage: www.elsevier.com/locate/apsusc

Full Length Article

# Assessing factors that determine adatom migration and clustering on a thin film oxide; $Pt_1$ and $Rh_1$ on the "29" $Cu_xO$/Cu(1 1 1) surface

Nisa Ulumuddin [a], Volkan Çınar [b], Alex C. Schilling [b], Adrian Hunt [c], Iradwikanari Waluyo [c,*], E. Charles H. Sykes [b,*], Jean-Sabin McEwen [a,d,e,f,g,*]

[a] The Gene and Linda Voiland School of Chemical Engineering and Bioengineering, Washington State University, WA 99164, United States
[b] Department of Chemistry, Tufts University, Medford, MA 02155, United States
[c] National Synchrotron Light Source II, Brookhaven National Laboratory, Upton, NY 11973, United States
[d] Department of Physics and Astronomy, Washington State University, Pullman, WA 99164, United States
[e] Department of Chemistry, Washington State University, Pullman, WA 99164, United States
[f] Institute for Integrated Catalysis, Pacific Northwest National Laboratory, Richland, WA 99352, United States
[g] Department of Biological Systems Engineering, Washington State University, Pullman, WA 99164, United States

ARTICLE INFO

*Keywords:*
Single-site catalysts
Stability
Surface science
Support effects
Density functional theory

ABSTRACT

The dynamical nature of single-site catalysts under non-equilibrium conditions poses significant challenges in the full characterization of their active sites. The "29" oxide is a thin $Cu_xO$ film grown on Cu(1 1 1) which provides a well-defined surface on which to study the structure and chemistry of atomically dispersed precious metals. A combination of experimental and first-principles approaches is used to investigate the factors that influence the mobility of metal adatoms and their clustering tendencies. Our work elucidates how a homogenous coordination environment of neutral single-atoms can be obtained when its tendency to break oxide bonds within its vicinity is low. We demonstrate that this in turn affects the chemical activity of atomically dispersed species on thin-film oxides, as defects on the oxide would in fact allow such species to be more accessible to CO. We thus highlight the importance of understanding the relationship between defects and atomically dispersed active sites upon designing single-site catalysts.

## 1. Introduction

Precious metals are critical components in many heterogeneous catalysts in the chemical industry, with applications ranging from energy production, chemical conversion, and automotive exhaust gas treatment.[1,2] Their thermal stability under reaction conditions and their high selectivity to specific reactions has made them indispensable to the chemical industry.[3] However, given the scarcity of precious metals in nature, their cost can be a significant factor in catalyst design. Supported atomically dispersed precious metals offer a new approach to catalyst design that minimizes the amount of precious metals required.[4] Additionally, the metal-support interactions in single-site catalysts are often unique with respect to their corresponding nanoparticle or bulk metal catalysts, which can potentially provide high product selectivity and atom efficiency.[5] The chemical and physical properties of single-site catalysts are susceptible to their local environment, as the support directly modulates their electronic structure and, consequently, their stability and chemical activity.[6]

Noble metals can react with loosely bound oxygen in reducible oxides to lower the activation barriers for various reactions.[4,7–10] They often exhibit enhanced catalytic activity in their cationic form with adjacent O ligands. Atomically dispersed catalysts may be the solution to the 150 °C challenge posed by the U.S. DRIVE [11], as more and more combinations of oxide-supported single-atom noble metals have been shown to lower the light-off temperature for CO oxidation.[4,12–18] Recent work has demonstrated that supporting noble metals on Cu-based surfaces can potentially enhance chemical activities for various reactions. For example, on bulk $Cu_2O$(1 1 1), the presence of $Pd_1^+$ enables $H_2$ to be easily activated and allows atomic H to form hydroxyls with the surface, facilitating highly selective hydrogenation of terminal alkynes.[19] Pt-doped $Cu_2O$ nanoparticles (NP) enhances CO oxidation activity by providing stronger anchoring sites and reducing the activation

* Corresponding authors at: The Gene and Linda Voiland School of Chemical Engineering and Bioengineering, Washington State University, WA 99164, United States (J.-S. McEwen).
*E-mail addresses:* iwaluyo@bnl.gov (I. Waluyo), charles.sykes@tufts.edu (E.C.H. Sykes), js.mcewen@wsu.edu (J.-S. McEwen).

https://doi.org/10.1016/j.apsusc.2023.157145
Received 14 March 2023; Accepted 25 March 2023
Available online 7 April 2023

barrier for the underlying mechanism.[10,20] Similarly, Rh/$Cu_2O$ NP provide catalytically active sites for hydroformylation reactions.[21]

Identifying how noble metal single-site catalysts interact synergistically with the support is a multidimensional problem.[22,23] Transitional interfaces are also essential to study because catalyst surfaces are always exposed to fluctuating oxidation conditions and are often not in equilibrium.[24] The study of active sites are often aided by DFT-based calculations and surface science-based approaches involving single-facet model surfaces.[8,25–27] Model surfaces are useful because they are composed of regular lattice sites, facilitating detailed metal-support interaction studies. While these models do not necessarily capture the heterogeneous and multifaceted nature of a catalyst, the well-defined coordination environments allow us to narrow our investigation to one variable at a time, and its complexity can be increased systematically.

In this contribution, we concentrate our efforts on the "29" copper surface oxide, a well-defined epitaxial copper oxide thin film, to assist our understanding of the underlying mechanisms and characteristics of single-atoms on transitional, $Cu_2O(1\,1\,1)$-like surfaces.[10,20,28] Owing to the atomic thickness of the "29" oxide, the surface provides an interface where the thin-film copper oxide covers a metallic Cu substrate. This models a Cu surface that is partially oxidized or is at an early stage of oxidation. It may also be relevant for strongly reduced $Cu_2O$ catalysts. The role of interfaces within thin oxide films is also technologically relevant for magnetic tunnel junctions, as well as dielectrics in electronic devices.[29–32] Therefore, understanding how metal atoms interact with thin-film oxide supports provides important fundamental information of use in many related systems.

The "29" oxide unit cell is composed of a Cu(1 1 1) substrate supporting an atomic layer of 6O-Cu–O rings, with an O adatom in the center of 5 of these rings.[28] Its surface rings structurally resemble the O-Cu–O ridges on $Cu_2O(1\,1\,1)$, a stable facet found under $O_2$ rich conditions.[10,21,33] It is well-ordered under ultrahigh vacuum (UHV) conditions, before and after temperature programmed desorption (TPD) experiments, allowing theorists to investigate atomic scale changes in the active site structure using DFT-based models.[34,35] The DFT-based models have been proven to be a useful platform for comparing the Preferential Oxidation (PROX) barriers between undoped and Pt-doped thin $Cu_xO$ [10] and predicting the water–gas shift [36] and CO oxidation [20] mechanisms.

The differences within the activities and distributions of Rh and Pt atoms were used as a baseline comparison to understand what drives the mobility and clustering of atoms on the "29" oxide. Scanning Tunneling Microscopy (STM) images reveal that the Rh supported on the "29" oxide are a mixture of clusters and single atoms at extremely low loadings (~0.5% of a monolayer (ML)) while Pt atoms exist exclusively as single atoms even up to a coverage of 2% of a monolayer (ML).[20] Our DFT simulation work provides insight as to why the features of the Pt and Rh species vary and determines that the non-uniformity of the coordination environment of Rh species is highly driven by the higher oxophilicity of Rh species causing more defects to form on the oxide. We consequently found that oxophilicity plays an important role in allowing Rh atoms to move across the surface more freely, allowing more metastable states to be accessible at low temperatures. In contrast, the oxide rings surrounding Pt single-atoms break at relatively higher energies. X-ray photoelectron spectroscopy (XPS) reveals that the ability of Rh to cause defects to the oxide in turn allows Rh to be more accessible to CO in comparison to Pt. We thus highlight the importance of understanding the relationship between defects and single-atom active sites upon designing single-site catalysts.

## 2. Methods

### 2.1. Computational methods

All electronic structure calculations were conducted using density functional theory (DFT) implemented in the Vienna *Ab initio* Simulation Package (VASP).[37,38] A plane wave basis was used, using the Projector Augmented Wave (PAW) potentials released in 2015 [39], to model the one-electron orbital wavefunctions making up the electron density.[40] The Cu $3p^6$, $3d^{10}$ and $4s^1$, O $2s^2$ and $2p^4$, Rh $4d^8$ and $5s^1$, and Pt $5d^9$ and $6\,s^1$ electrons are modeled as valence states. We also applied a kinetic cutoff energy of 500 eV to the plane wave basis. Following the structurally accurate "29" oxide model determined by Therrien *et al.* [28], we have used the Perdew, Burke, and Ernzerhof (PBE) exchange–correlation functional within the generalized gradient approximation (GGA) level of theory.[41] All calculations were spin-polarized, resulting in a total magnetic moment of 0. A Gaussian smearing method with a width of 0.2 eV was applied to treat the Fermi level. All geometry optimization calculations were conducted using the conjugate-gradient algorithm, set to converge after differences in energy and force reach $10^{-6}$ eV and $10^{-2}$ eV/Å, respectively.

The "29" oxide model used in this study was benchmarked to experimental STM in previous studies by Therrien *et al.*[28] The "29" oxide consists of an atomic film of $Cu_xO$ rings adsorbed on a 4-layer Cu (111) slab, where oxygen adatoms rest in the center of 5 out of 6 rings. Structurally, the ridges of the $Cu_xO$ rings resemble the surface rings of $Cu_2O(1\,1\,1)$. The unit cell of the underlying Cu(1 1 1) substrate for the "29" oxide is a $\sqrt{13}R46.1$Å $\times$ $7R21.8$Å supercell of Cu(1 1 1), 29 times larger than the original unit cell of Cu(1 1 1). The "29" oxide unit cell is approximately 18 Å by 19 Å. During geometry optimizations, the bottom two Cu layers were fixed in their positions while the top two layers as well as the oxide layer were allowed to relax. "Charge sloshing" between periodic unit cells in the z-direction was minimized by the addition of a 15 Å vacuum layer.[42] An optimal k-point sampling of $1 \times 2 \times 1$ using the Monkhorst-Pack [43] grid was used to sample the Brillouin zone. The schematic of the "29" oxide unit cell is shown in Fig. 1.

As the total DFT energy is arbitrary, we represented the potential energy surface (PES) minima as relative energies to the most energetically favorable structure, which we refer to as the global minimum (GM). The relative energy is calculated as Equation (1):

$$E_{\mathrm{rel}} = E - E_{\mathrm{GM}} \tag{1}$$

where $E$ is the total DFT energy and $E_{\mathrm{GM}}$ is the most energetically favorable structure.

Various calculations assessed the Pt and Rh adatom's interaction with the "29" oxide. The binding energy of the metal (M) adatom to the "29" oxide is calculated through Equation (2):

$$E_{\mathrm{bind}} = E_{\mathrm{M+29ox}} - (E_{\mathrm{29ox}} + E_{\mathrm{M.gas}}) \tag{2}$$

where $E_{\mathrm{M+29ox}}$ is the total energy of the metal adatom on the "29" oxide, $E_{\mathrm{29ox}}$ is the total energy of the clean "29" oxide slab, and $E_{\mathrm{M,gas}}$ is the energy of an isolated metal atom in the gas phase. Similarly, the CO adsorption energy is presented in Equation (3):

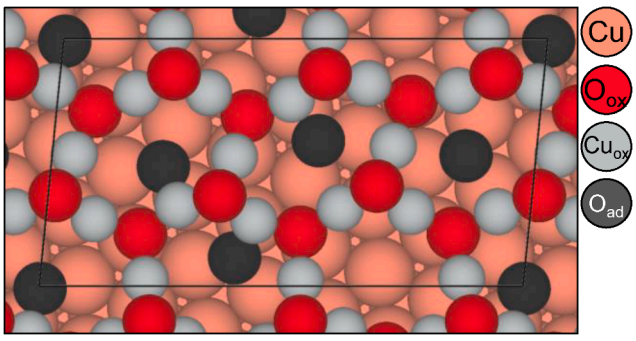


**Fig. 1.** DFT-based model of the "29" oxide unit cell. The atoms are color-coded: Salmon (Cu), Red ($O_{oxide}$), Grey ($Cu_{oxide}$), and Black ($O_{adatom}$).

$$E_{ads} = E_{CO+29ox} - (E_{29ox} + E_{CO,gas}) \quad (3)$$

where $E_{CO+29ox}$ is the total energy of the CO-adsorbed surface, $E_{29ox}$ is the total energy without CO adsorbed and $E_{CO,gas}$ is the gas-phase energy of an isolated CO molecule.

The Bader charge can be used as an indicator for the charge state of the adatom.[44] The partial Bader charge is shown in Equation (4), where a negative Bader charge correlates to a more negatively charged adatom.

$$Q = Q_{total} - Q_{neutral} \quad (4)$$

where $Q_{total}$ is the total Bader charge implemented using Henkelman's algorithm [45] and $Q_{neutral}$ is the number of valence electrons specified by the PAW potential.[39]

Upon the movement of an adatom across the "29" oxide, the oxide rings within its vicinity can be affected through repulsive and attractive interactions. A measure of the oxide distortion energy provides insights into the extent of structural changes toward the oxide with respect to the ground state of a clean "29" oxide surface. The distortion energy is quantified by Equation (5), using the same logic as Refs [46–48]:

$$E_{dist} = E_{29ox}^{distr} - E_{29ox}^{relaxed} \quad (5)$$

where $E_{29ox}^{distr}$ is obtained through a static calculation of the clean "29" oxide system that the adatom has distorted, and $E_{29ox}^{relaxed}$ is the original ground-state of the system before the adatom distorted it.

The minimum energy pathway and transition state calculations involved during the migration of an adatom across the "29" oxide were computed using a combination of Climbing Image Nudged Elastic Band (CINEB) [49,50] and Dimer [51] methods. The CINEB algorithm was used to determine the energy pathway between each initial and final state pair and their corresponding transition state structure. The quick-min algorithm [52] was implemented to handle force optimizations along the pathway with maximum finite difference step sizes of 0.05 Å. As some transition states predicted by the CINEB method indicated the presence of multiple imaginary vibrational modes, the Dimer method was additionally carried out to further optimize or validate the search. Using a combination of the two methods, all transition state structures were verified to possess only one imaginary vibrational mode. During the vibrational mode analyses, all Cu(1 1 1) atoms were held fixed, so only the modes of the "29" oxide layer and the metal adatom were analyzed.

To compare the favorability of dimer formation for Pt and Rh adatoms, we have simulated three hypothetical scenarios (Dimer_A, SA_AB, and Dimer_B, where SA_AB is short for "single-atoms" on Site A and Site B). The reaction energies of the three dimer configurations (Dimer_A, SA_AB, and Dimer_B) with respect to isolated single-atom configurations (Site A and Site B) were calculated. We categorized the dimer formation energies for the Dimer_A and Dimer_B configurations as $\Delta E_{pair\_i}$ and the configuration SA_AB as $\Delta E_{sepa,}$ as shown in Fig. 2. The equations for $\Delta E_{sepa}$ and $\Delta E_{pair\_i}$ are shown in Equation (6) and (7).

$$\Delta E_{sepa} = E_{clean\_29ox} + E_{SA\_AB} - (E_{SiteA} + E_{SiteB}) \quad (6)$$

$$\Delta E_{pair\_i} = E_{clean\_29ox} + E_{Dimer\_i} - 2E_{Site_i}, i = A, B \quad (7)$$

where $E_{clean\_29ox}$ is energy of the clean "29" oxide without the adatom, $E_{Dimer\_i}$ is the energy of the dimer configuration, $E_{Site\_i}$ is the energy of single-atom configuration and subscript $i$ is the site number A or B.

Scanning Tunneling Microscopy (STM) images were simulated by running an additional set of static calculations aimed to process the partial charge densities of the optimized structure in p4vasp. The bias voltage applied to the surface is implemented by evaluating only the corresponding range of bands within the system. In these simulations, the number of grid points in the Fast Fourier Transform grid is doubled with respect to the default value set in VASP for higher accuracy.

### 2.2. Experimental methods

For the STM experiments the Cu(1 1 1) crystal was sputtered with Ar ions and annealed to 750 K in a preparation chamber with a base pressure of $2 \times 10^{-10}$ mbar. The "29" oxide was grown by exposing the Cu(1 1 1) crystal, held at 650 K ± 20 K and $5 \times 10^{-6}$ mbar $O_2$, for 3 min. Then, the sample was transferred in UHV to the STM chamber (Omicron Nanotechnology) with a base pressure of $1 \times 10^{-11}$ mbar and into the STM stage which was held at 80 K or 5 K for imaging. Afterwards, the sample was transferred to the adjacent preparation chamber for Rh or Pt deposition and brought back to STM to cool back down to 5 K and imaged at this temperature. Deposition of Pt and Rh on the 29-oxide surface was performed at a sample temperature ~ 200 K using a Focus GmbH EFM3 electron beam evaporator. The as-prepared surfaces were exposed to CO to prevent CO uptake from the background during the experiment. During these processes the samples were under UHV at all times and the order and timing of operations were the same. One monolayer is defined according to the packing density of Cu(1 1 1) which is $1.77 \times 10^{15}$ atoms/cm$^2$. Etched W tips were used to acquire the images and biases were reported with respect to the sample.

X-ray photoelectron spectroscopy (XPS) experiments were performed at the *In situ* and *Operando* Soft X-ray Spectroscopy (IOS/23-ID-2) beamline at the National Synchrotron Light Source II, Brookhaven National Laboratory. Details about the beamline and endstation have been described elsewhere. The Cu(1 1 1) crystal was cleaned with cycles of $Ar^+$ sputtering and annealing to 850 K until C and O were no longer detected by XPS. The "29" oxide was prepared using the same method as the STM experiment. Rh and Pt were deposited on the oxide at a sample temperature of 300 K using a SPECS EBE-4 electron beam evaporator, with the evaporation rate calibrated using a quartz crystal microbalance.

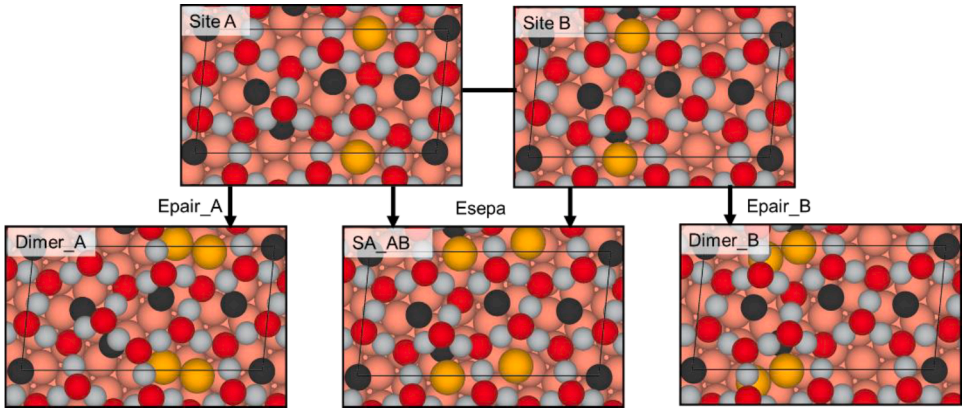


**Fig. 2.** Each dimer configurations linked to their initial states. The atoms are color coded: Salmon (Cu), Red (O), Grey (Cu), Black (O), Yellow (adatom).

C 1*s*, Rh 3*d*, and Pt 4*f* spectra were acquired at photon energies of 460 eV, 500 eV, and 250 eV, respectively. The binding energy was calibrated using the Fermi level measured at each photon energy.

## 3. Results and discussion

### 3.1. Comparison of Pt and Rh atom distribution using STM

Fig. 3A-C shows representative STM images of the clean "29" oxide, 0.5 % ML Pt on the "29" oxide, and 0.5% ML Rh on the "29" oxide, respectively, after deposition at ~ 200 K and cooling to 5 K for imaging. Before describing the appearance of the Pt and Rh deposited surfaces it is important to quantify any defects intrinsic to the "29" oxide surface so that they are not misassigned as adatoms. The protrusions seen in the STM image in panel A are the small number of defects intrinsic to the 29 oxide. [35] Previous studies termed these defects "dim" and "bright" defects. [35] The dim defects occur due to a missing O atom, whereas bright defects result from an additional Cu atom. The overall defect density of the clean "29" oxide was ~0.02% ML. [28] The STM image in Fig. 3A has four bright (labeled 2–5) and one (labeled 1) dim defect.

By visual inspection, these dim and bright spots look noticeably distinct from the features seen in images B and C. Specifically, for the STM image in Fig. 3B, the protrusions are uniformly sized, consistent with single Pt atoms. This atomic dispersion of Pt on the "29" $Cu_2O$ oxide was confirmed in previous work using STM and surface IR studies. [20] On the other hand, the protrusions seen in Fig. 3C have various sizes indicating that Rh exists as a mixture of single atoms and clusters on the "29" $Cu_2O$ oxide surface. A statistical analysis of the STM images

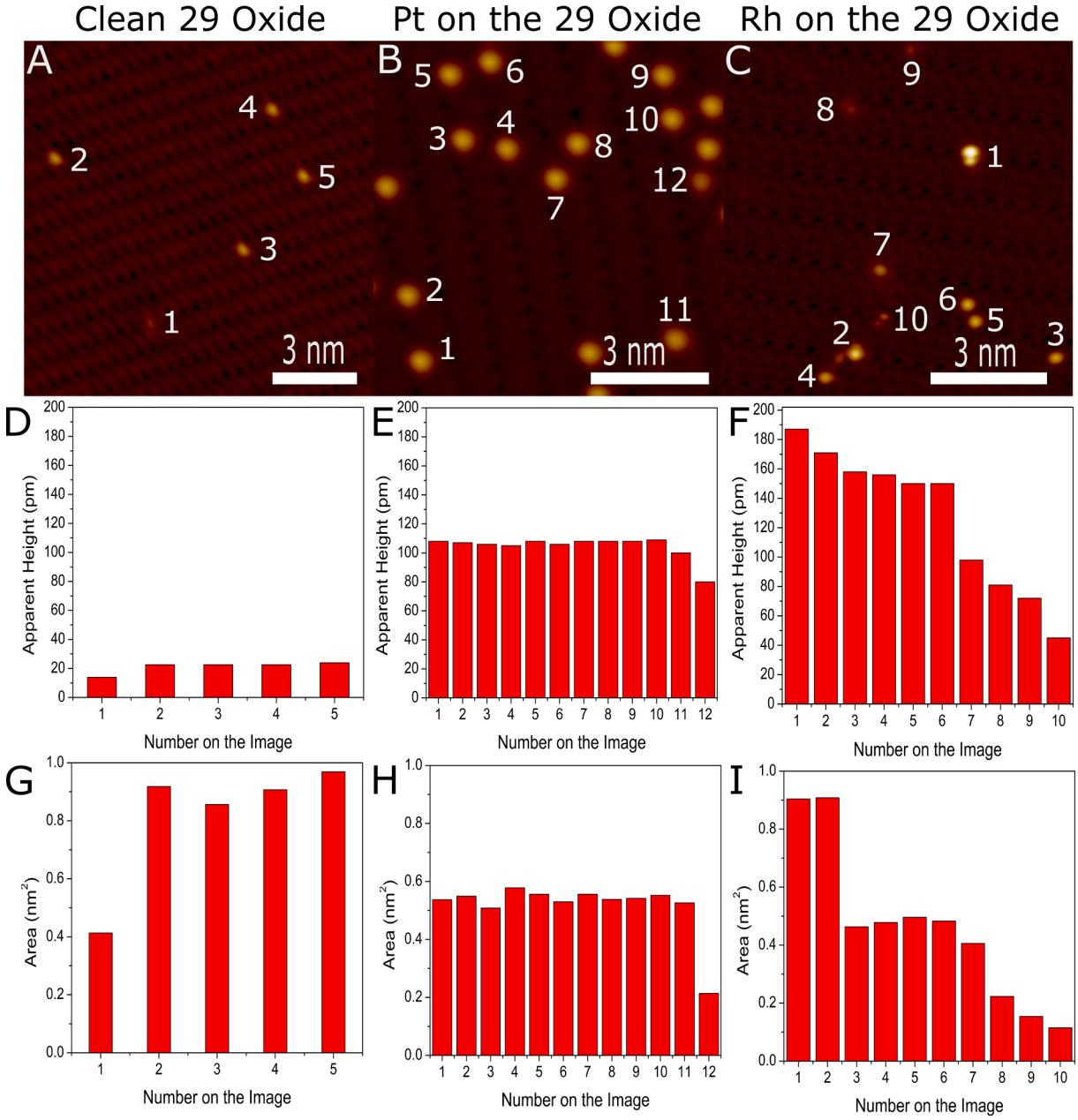


**Fig. 3.** (A) High-resolution STM image of defects commonly found on the clean "29" oxide. Number 1 shows a "dim" defect associated with an O vacancy and numbers 2–5 show "bright" defects associated with the presence of a Cu adatom.[35] The defect density of the as-prepared "29" oxide is very low, with a defect coverage of ~0.02% ML with respect to Cu(1 1 1). [28] Panels B and C are 5 K high-resolution STM images of 0.5% ML Pt on the "29" oxide and 0.5% ML Rh on the "29" oxide, respectively. Panels D-F are apparent height measurements of the features in the STM images A-C. G-I are footprint area measurements of the features in the STM images shown in panels A-C, respectively.

in Fig. 3A-C is shown in the panels below the STM images. It is clear from the apparent height of the 0.02% ML defects intrinsic to the "29" oxide (panel D) that they are different from the features observed after Pt and Rh deposition on the oxide (panels E and F). The Pt atoms have a uniform height of ~ 100 pm versus both types of defects which have an apparent height of ~ 20 pm.

Contrary to Pt, deposition of the same amount of Rh (0.5% ML) yields a wide distribution of particle sizes with apparent heights in the range 40–180 pm as seen in panel F, providing evidence for Rh existing as a mixture of single atoms and clusters. Other particles in panel F were found either equal or smaller, yet still distinct from the defects intrinsic to the "29" oxide. These conclusions are further supported by the measurements of the area or "footprint" of the defects/atoms/clusters seen in panels G-I. As we will later show, protrusions with small "footprint" areas but relatively high apparent heights may be assigned to a variation of Rh single-atom species, as they can position themselves underneath or above the oxide layer even at low temperatures, causing protrusions of single-site Rh to be more variable in height and area. Again, the isolated Pt atoms all have the same area size, whereas the Rh single-atoms and clusters show a range of area sizes. These STM experiments and their statistical analysis provide evidence that the same coverage (0.5% ML) of Pt and Rh on the "29" oxide leads to very different structures. While Pt exists on the surface as only single atoms, Rh exists as a mixture of small clusters and single atoms.

### 3.2. Non-Uniformity of Single-Atom sites on the "29" oxide

In order to investigate the heterogeneity of the Rh species in comparison to Pt, the potential energy surface of an adatom on the "29" oxide was investigated within our DFT-based model by plotting the relative energy distribution of 31 single-atom adsorption sites (PES minima) on the "29" oxide listed in Figs. S1 and S2. While many adsorption sites are structurally identical between Rh and Pt, we found that they can be energetically different. In other words, sites which may be accessible to Rh atoms may not be accessible to Pt atoms, and vice versa. We have categorized the PES minima into 3 categories, the "Center" sites, "Under-oxide" sites, and the "Over-oxide" sites (Fig. 4). The occurrence of each category is then presented on the relative energy distribution graph shown in Fig. 4. The PES minima are grouped within intervals of 0.15 eV, between relative energies of 0 and 3 eV, with respect to the lowest-energy adsorption site, the global minimum (GM). Occupation of sites within the center of the oxide ring will be referred to as Center sites. Under-oxide sites occur underneath the ridges of the oxide ring, potentially causing strain within the oxide rings by pushing it upward and away from the Cu(1 1 1) substrate. Lastly, Over-oxide sites typically consist of an adatom directly coordinated on top of the oxide ring, lacking direct contact with the Cu(1 1 1) substrate. Given that all the model parameters are kept constant throughout our simulations, the total DFT energy of a structure can be an indication of the structure's favorability. Lower energy correlates to a more stable coordination environment.

Fig. 4 shows that the energy distribution of the Rh adsorption sites for single atoms are clustered at relatively lower energies than Pt, an indication that more sites are accessible to the Rh single-atom especially at low temperature. We display a sample of the Center, Under-oxide and Over-oxide sites in Fig. 4. Center sites and Under-oxide sites generally lie below the mean relative DFT energy, which indicates that chemisorption with the Cu(1 1 1) surface provides stability to the adatom. Contact with Cu(1 1 1) makes the "29" oxide support distinct to bulk $Cu_2O$ surfaces. For instance, there are eight Rh adsorption sites within the 0–0.15 eV DFT energy range while only four sites for Pt. Fig. S4 further highlights that, as compared to Rh, the relative depth of the global minimum (GM) for single-atom Pt is lower with respect to other Pt adsorption minima. This implies that the preference to occupy the GM state is more acute for Pt single-atoms, justifying why we would expect higher non-uniformity of Rh single-atom species observed on the "29" oxide.

Since single site Rh can theoretically occupy Center, Under-oxide and Over-oxide sites even with low energies, the protrusions induced by the presence of single site Rh can be nonuniform. Fig. 5 displays samples of simulated STM of the sites that are within the 0–0.15 eV range for the isolated Rh atom with all its simulation parameters identical. The brighter areas are associated to elements that are higher in elevation from the Cu(1 1 1) surface. The position of the single-site Rh are annotated by a green circle of each simulated STM. Fig. 5a and b

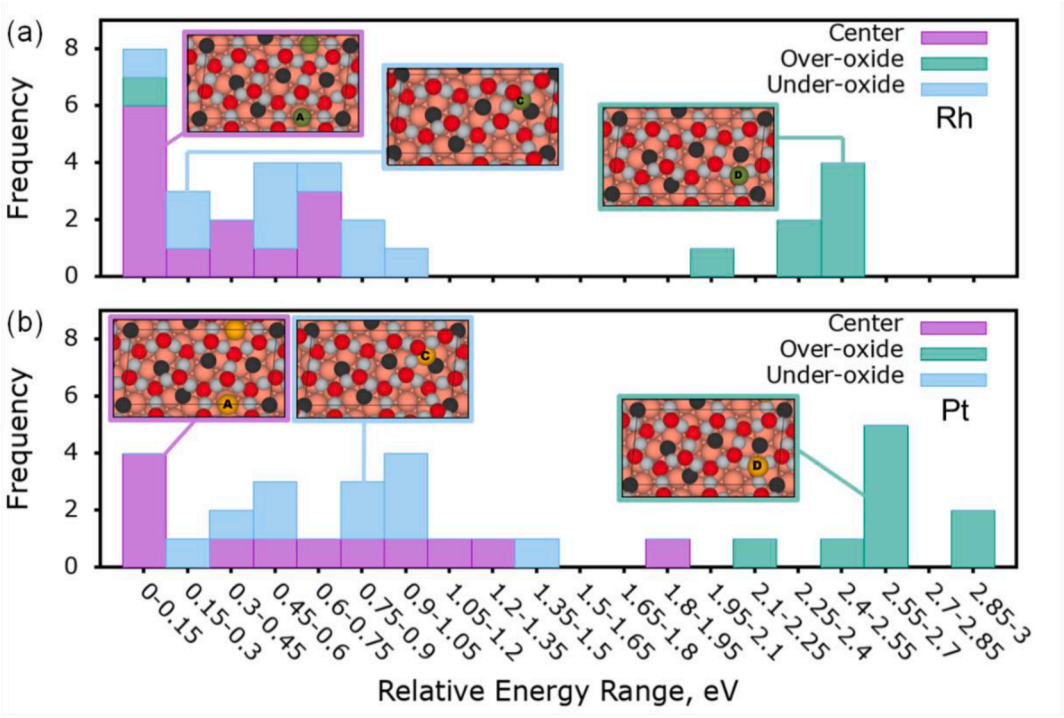


**Fig. 4.** Relative energy distribution of the potential energy minima of 31 adsorption sites of (a) $Rh_1$ and (b) $Pt_1$ on the "29" oxide.

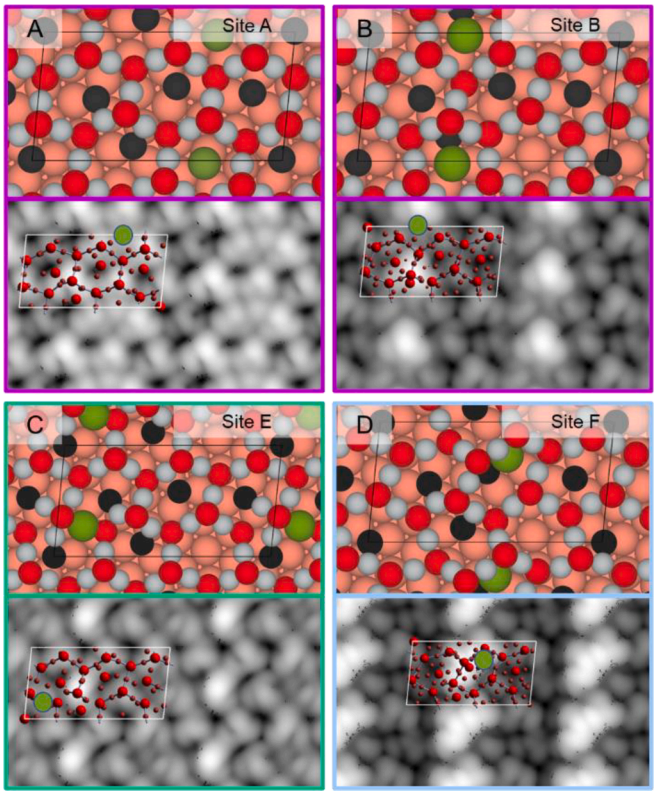


**Fig. 5.** Samples of simulated STM of Center (purple), Over-oxide (light green), and Under-oxide (light blue) isolated $Rh_1$ positions on the "29" oxide within the 0–0.15 eV range of Fig. 4A. The green circle in the simulated STM denote the position of the single-site Rh within that unit cell. The STM simulations were run with bias voltages of 0.5 V/Å. Every image was generated in p4vasp.

display the protrusions of $Rh_1$ occupying a Center site. The single-site Rh that occupies an empty $Cu_xO$ ring (Site A) has a relatively wider but dimmer bright area as compared to the single-site Rh which occupies an $O_{adatom}$-containing $Cu_xO$ ring (Site B). This is because the Rh single-atom is at the same level of the oxide layer, and thus the collective brightness of the Cu–O-Cu ridges and $Rh_1$ spread over a wider area. On Site B, the presence of the Rh single-atom displaces the $O_{adatom}$, which causes a Cu–O-Cu ridge to protrude outward, causing the bright spot to be mainly associated to this protrusion. Similarly, Fig. 5c and d exhibit different footprint areas associated to the presence of Rh single atoms when the Rh is underneath or at the same level of the $Cu_xO$ rings. Our simulations show that the bright spots induced by the presence of single-site Rh are in fact produced by a lifted or protruded adjacent Cu–O-Cu ridge. Consequently, the presence of single-site Rh can be manifested as a variety of "footprints" on an STM image. Our simulations agree with the experimental observations that the footprints of Rh species are nonuniform even for its single atoms.

### 3.3. Driving factors to atom mobility

The manner in which the adatom interacts with the "29" oxide plays a significant role in adatom mobility. To elucidate the driving factors to adatom mobility, we have simulated a migration pathway starting from Site A to Site B. The energy difference for this process is relatively more exothermic for Rh, at −0.18 eV, relative to Pt at 0.45 eV. These numbers reflect how Pt much prefers to stay in Site A while Rh has little preference to be on either site. In comparison to migration through hopping above the oxide, the migration pathway by diffusing underneath the $CuO_x$ rings is less energetically costly as the adatom can maintain coordination with Cu(1 1 1) (see Supplemental Information for calculation details). The migration pathway is divided into 2, where the first half is displayed in Fig. 6 and the second half is displayed in Fig. 7.

The rate-limiting step for the migration of the adatom between Sites A and B have energy barriers of 0.68 eV and 0.45 eV for Pt and Rh, respectively. This rate-limiting step occurs in the first elementary step shown in Fig. 6, as the adatom passes underneath the oxide, pushing the ring outward. The structural distortion of the oxide is reflected by its increase in the distortion energy, as seen by the purple line in Fig. 6b. While the induced oxide distortion is energetically and structurally comparable between the two cases, the rate-limiting activation barriers of this process differ by 0.23 eV, with the Pt adatom overcoming a higher barrier. The correlation between oxide distortion energy and the elementary steps' activation barriers indicates that the adatom's ability to distort the oxide with low energy costs allows the adatom to migrate more easily. We also found more barrierless elementary steps for the migration of a Rh single atom (Fig. 6a and 7a) than for a Pt single atom, which is further support that its PES is shallower than that of a Pt single atom. We argue that the relatively stronger binding to Cu(1 1 1) (shown in Table 1) of a Pt single atom constrains Pt to deeper adsorption wells and therefore make them less mobile.

The charge state of the adatom during its migration steps was tracked by performing a Bader charge analysis (Fig. 6b) to investigate whether the adatom exchanges electrons with the surrounding oxide. Although a more negative partial Bader charge was observed on the Pt adatom, previous works have determined that the isolated Pt [20] and Rh [53] adatoms are neutral. It is well-established that while the Bader charge directly correlates with the oxidation state, it is not enough to calculate the actual oxidation state without correlating these results with an experiment.[44] Since the charge state of the adatom is unchanged during the rate-limiting step, single-atom mobility is not driven by charge transfer.

The second half of the migration pathway is displayed in Fig. 7. In this phase, the single-atom switches coordination from the $Cu_xO$ ring to the $O_{adatom.}$ The barriers associated to this half are relatively lower for both the Rh and Pt single-atoms (Fig. 7a) because the oxide ring is allowed to relax after breaking its connection with the reactive metal adatom. Concurrently, we also see a drop in the oxide distortion energy as each adatom coordinates with $O_{adatom}$ and breaks its bonds with the $Cu_xO$ ring (Fig. 7b). This is coherent with our argument that the energy cost to distort the oxide is the determining factor to atom mobility. Loss of adatom charge was in turn observed, with a Bader charge loss of ~ 0.35 *e,* reflecting charge transfer from the reactive single-atom to the $O_{adatom}$ (Fig. 7c). Upon arriving on Site B, the adatom finally coordinates solely with the $O_{adatom}$ (Images 11 and 10 in Fig. 7c). Our results imply that the oxophilic character of the Pt and Rh adatoms aid in lowering the diffusion energy, as the bond formation with one oxygen to the next helped the adatom migrate with low barriers. Table 1 displays a comparison of Pt and Rh binding to the Cu(1 1 1) surface in the presence and in the absence of the oxide. The last column displays the energy difference caused by the presence of the oxide. From this data, we can see that the adsorption of Pt is more strongly governed by its bonding with Cu as compared to Rh.

To summarize thus far, our DFT simulations validate what was observed experimentally and provide insights as to what causes the coordination of single atoms to be more variable when adsorbed on a surface oxide such as the "29" oxide. Bonding with surface oxygen (either $O_{oxide}$ or $O_{adatom}$) weakens binding to Cu and allows the adatom to be mobile. Rh adatoms easily form new bonds with the surface oxide, allowing more variety of metastable states to take place. This contribution of metal oxophilicity toward adatom mobility is unlike what is normally observed for single atoms on bulk oxide surfaces, where oxophilicity typically correlates to higher stability of its single atoms. Since the oxide layer on the "29" oxide is adsorbed on metallic Cu, the factors which drive atom mobility can be significantly different than on bulk oxides.

To ensure that Rh is indeed more oxophilic than Pt even in its bulk metallic state, a comparison of cohesive energies is presented in Table 2.

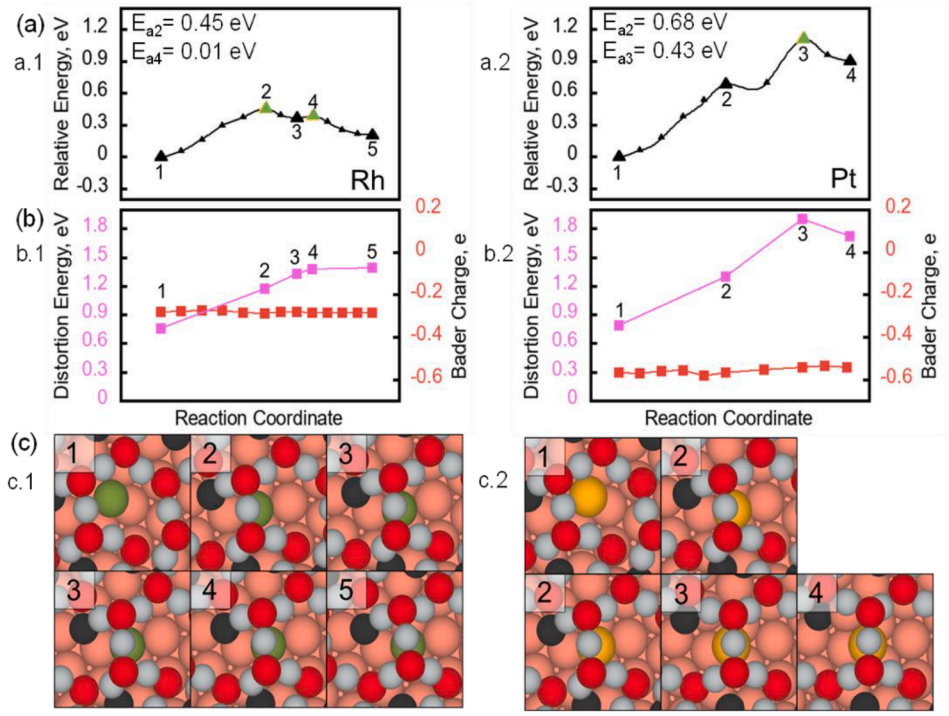


**Fig. 6.** (a) The energy pathway of adatom hopping from image 1 to image 5 in (c) for Rh (a.1, c.1) and Pt (a.2,c.2) adatoms. Color-coded in green are the transition states, where their activation energies are specified in a subset. (b) The progression of oxide-layer distortion energy (purple) and partial Bader charge (red) during adatom diffusion from image 1 to image 5 (Rh: b.1, Pt: b.2) The atoms are color coded: Salmon (Cu), Red (O), Grey (Cu), Black (O), Green (Rh), Yellow (Pt).

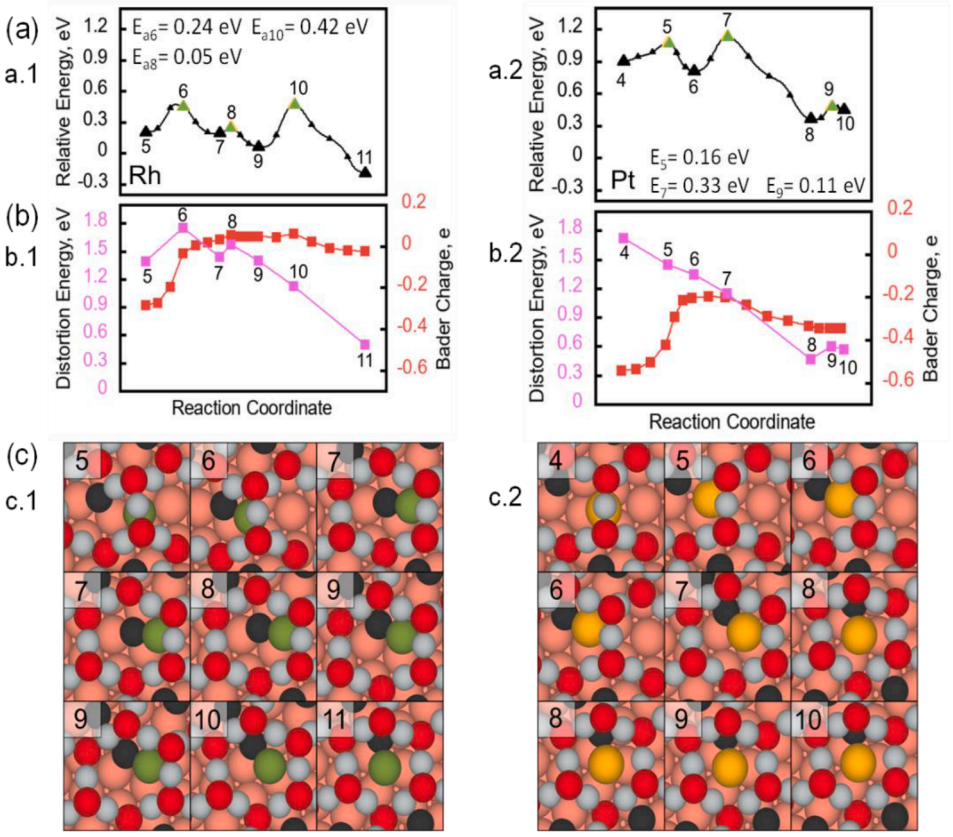


**Fig. 7.** (a) The energy pathway of adatom hopping from image 5 to image 11 in (c) for Rh (a.1, c.1) and Pt (a.2,c.2) adatoms. Color-coded in green is the transition states, where their activation energies are labeled in a subset. (b) The progression of oxide-layer distortion energy (purple) and partial Bader charge (red) during adatom diffusion from image 5 to image 11 (Rh: b.1, Pt: b.2) The atoms are color-coded: Salmon (Cu), Red (O), Grey (Cu), Black (O), Green (Rh), Yellow (Pt).

**Table 1**
Comparison of Pt and Rh adatom binding energy to the Cu(1 1 1) and the "29" Oxide (on Site 25) with the binding energy difference on the fourth column.

| Metal | Cu(1 1 1), eV | "29" oxide, eV | Δ Binding Energy, eV |
|---|---|---|---|
| Pt | −4.37 | −5.03 | 0.66 |
| Rh | −3.85 | −4.71 | 0.86 |

**Table 2**
Comparison of $MO_2$ dissociation temperature and $Cu_3M$ cohesive energy (M = Rh,Pt).

| Metal (M) | Dissociation Temperature, °C (atmospheric conditions)[54] $MO_2 \rightarrow M + O_2$ | Cohesive Energy of $Cu_3M$, eV |
|---|---|---|
| Rh | 1050 | −4.00 |
| Pt | 650 | −4.12 |

The decomposition temperature of their $MO_2$ oxides (M = Rh, Pt) is a descriptor for their oxophilicity and the DFT-calculated cohesive energy of $Cu_3M$ bulk alloy crystals (see SI for calculation details) is an indicator of Cu-M strength. The higher oxophilic character of Rh is reflected by the higher decomposition temperature of $RhO_2$.[54] The cohesive energy of cubic $Cu_3Rh$ and $Cu_3Pt$ crystals differ by 0.12 eV/atom, with $Cu_3Pt$ exhibiting stronger cohesion. The difference in cohesive energy is in support of why the binding of Pt on clean Cu(1 1 1) is stronger than that of Rh by 0.52 eV, previously shown Table 1.

### 3.4. Driving factors to dimer formation

One needs to consider the cohesive strength between like-adatoms in the context of cluster formation as they are driven by a combination of atom mobility and sufficient cohesive strength between the adatoms. In the literature example of Pd on $Fe_2O_3$, several Pd atoms needed to be within close vicinity to form a cluster [55] and the interaction between two Pd adatoms was not strong enough to create a dimer at room temperature under UHV.[55] Here, we have considered the formation of the smallest cluster possible, a dimer. The aggregation of two adatoms and their formation energies with respect to an isolated adatom is displayed in Fig. 8.

Sites A and B were again used as representative sites for the adsorption on the empty ring and the ring containing an $O_{adatom}$, respectively. Interestingly, forming the SA_AB configuration, where the oxide physically separates two isolated adatoms, has no greater favorability than the isolation of two adatoms that are separated by the unit cell. Their interaction energies are much more considerable within the Dimer_A and Dimer_B configurations. Our calculations demonstrate that the formation energies of configurations Dimer_A and Dimer_B are both more endothermic for Pt. The higher favorability of forming Rh dimers can be partly explained by the higher cohesion energies between Rh atoms, relative to that between Pt atoms, as reflected by their bulk cohesive energies in Table 3. The calculation details to calculating cohesive energy of bulk metals is entailed in the SI.

An interesting effect of the higher oxophilicity of Rh is again displayed during the formation of dimers. Due to strong interactions with the oxide, the $Cu_xO$ layer is more flexible in the presence of Rh. As the Rh dimers coalesce, the oxide ring around it distorts and forms O-Rh bonds. This contrasts with how the oxide stays intact around Pt dimers, without the formation of new bonds, accommodating more strain. We infer that the higher flexibility of the oxide around Rh atoms is the main reason why various Rh clusters form under conditions where Pt single-atoms can be exclusively isolated. The binding energy comparison for every representative site is listed in Table 3, showing that the energetic minima of Rh dimers are consistently lower than Pt dimers.

### 3.5. Effect of CO toward atom mobility

The potential effects of CO toward the distributions of Pt and Rh species on the "29" oxide was investigated. The CO-induced mobility of Rh species on the "29" oxide was highlighted by Schilling et al.[53], where Rh atoms can mobilize such that single atoms can split from clusters, forming isolated single atom species. Atom mobility and changes in surface composition are often enhanced upon the adsorption of gas-phase species.[16,55–57] The same representative sites were selected, namely Site A and Site B, to compare the binding strengths of the metal adatom to the surface upon the adsorption of CO.

In Fig. 9a, the CO-induced bond lengthening between a metal adatom to the "29" oxide surface is displayed. Unsurprisingly, the adsorption of CO lengthens and weakens the metal adatom's binding to the surface.[58] However, interestingly, the Rh adatom (green) is lifted off the surface higher than Pt on both sites (Fig. 9a). This is in support of the CO-induced mobility of Rh atoms observed by Schilling *et al.*[53] Fig. 9b indicates that CO would bind to Site A in equal strength to Site B on the Rh-adsorbed surface, assuming Rh is isolated as single atoms. This means that in the presence of CO, Rh single-atoms are energetically indistinguishable on Sites A and B despite being coordinatively different. This is not the case for the Pt adatom. We hypothesize that, in comparison to the Pt-deposited surface, more Rh sites are energetically

**Table 3**
Comparison of the cohesive energy within bulk Rh and Pt fcc crystals.

| Properties | Rh | Pt |
|---|---|---|
| **Bulk Cohesion Energy, eV** | −6.28 | −5.85 |
| **Binding Energy of Each Atom within Dimer_B, eV/atom** | −4.65 | −4.57 |
| **Binding Energy of Each Atom within SA_AB, eV/atom** | −4.75 | −4.92 |
| **Binding Energy of Each Atom within Dimer_A, eV/atom** | −5.24 | −4.66 |

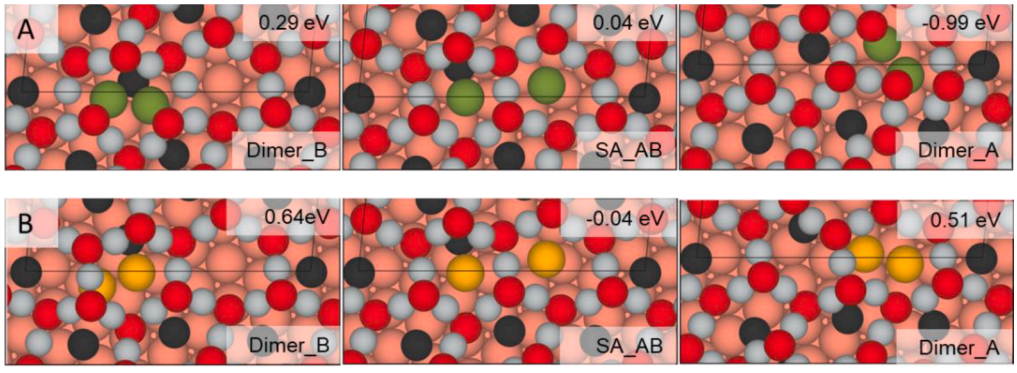


**Fig. 8.** Formation energies to aggregate Rh (A) and Pt (B) adatoms on Site 15 (left) and Site 25 (right) relative to an isolated atom within the "29" oxide unit cell. The atoms are color-coded: Salmon (Cu), Red (O), Grey (Cu), Black (O), Green (Rh), Yellow (Pt).

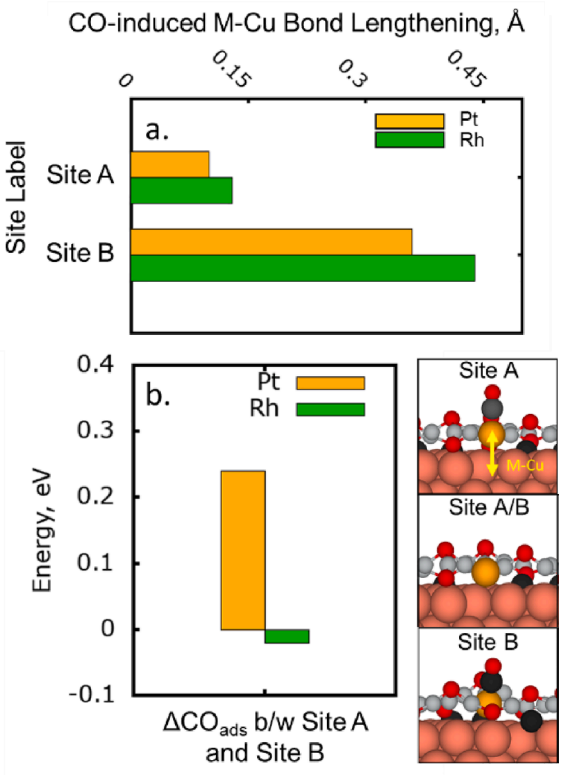


**Fig. 9.** (a) CO-induced bond lengthening on Site A and B (b) The difference in CO adsorption energy between Sites A and B. The side-view schematics of Sites A and B are shown on the right panels. The atoms are color-coded: Salmon (Cu), Red ($O_{oxide}$), Grey (Cu), Black ($O_{adatom}$), Yellow (Metal Adatom).

indistinguishable even in the presence of CO.

### 3.6. Comparison of CO adsorption on Pt and Rh using XPS

XPS was used to probe the adsorption of CO on 1% Pt and Rh deposited on the "29" $Cu_2O$. Fig. 10a shows the C 1*s* spectra measured after the surfaces were exposed to $1 \times 10^{-4}$ Torr of CO for 30 s at 300 K. Two peaks arising from adsorbed CO can be observed on Rh deposited on the "29" oxide (upper spectrum). We previously assigned the peak at 286.2 eV to CO adsorbed on single Rh sites and the one at 285.6 eV to CO adsorbed on Rh clusters [53] based on comparison with CO adsorption on atop and threefold hollow sites of Rh(1 1 1), respectively.[59] The observation of CO adsorption on Rh single atoms and clusters supports the STM and DFT results. The shift in the Rh $3d_{5/2}$ binding energy (BE) to higher energy, shown in Fig. 10b, confirms the presence of adsorbed CO on Rh sites. In contrast, CO adsorption was not observed on Pt deposited on the "29" oxide (Fig. 10a, lower spectrum). Fig. 10c shows that the Pt $4f_{7/2}$ spectra before and after CO exposure are identical with no observed BE shift due to adsorbed CO, which indicates that the Pt atoms are blocked from binding CO, likely by the oxide layer. This is similar to the case of the oxidation of Pt/Cu(1 1 1) SAA surface reported previously, where the formation of a complete oxide layer prevents the adsorption of CO on Pt.[60]

The observation of CO adsorption on Rh but not on Pt can be explained by the structural distortions of the "29" oxide layer caused by the oxophilic nature of Rh, as predicted by DFT calculations. Rh atoms likely introduce more defects to the oxide layer, thus allowing Rh atoms to sit in open areas of the distorted oxide, and therefore they are available to bind CO. On the other hand, at a deposition temperature of 300 K, higher than the 200 K used for the STM experiment, deposited Pt atoms likely diffused under the oxide layer without breaking Cu–O bonds and distorting the oxide, thus leaving the oxide layer intact, which then prevents CO adsorption on Pt. The diffusion of Pt under the "29" oxide at an elevated temperature was previously reported [20] and the tendency of Pt to form an alloy with the underlying metallic Cu is also consistent with the DFT result that shows the stronger cohesive energy between Pt and Cu.

## 4. Conclusions

Transitional interfaces are essential to study, given that catalyst surfaces are often exposed to fluctuating oxidation conditions and are often not in equilibrium.[24] The study of single atoms on the "29" copper oxide model system provides interesting insights toward a transitional Cu-based surface where a thin layer of $Cu_2O$(1 1 1)-like oxide adsorbs on Cu(1 1 1). Precious metal single atoms are stabilized on the "29" oxide surface as metal adatoms rather than cationic ions integrated within the $Cu_xO$ lattice, which makes the metal-support interaction on this model distinct from other bulk oxides.[20,53] In this work, we have identified the driving factors to atom mobility and clustering to understand the contrasting images of Rh and Pt atom distributions and accessibility to CO on the "29" oxide.

Comparing the binding, migration, and dimer formation of Pt and Rh adatoms facilitates an understanding of what enables Pt to remain isolated under the same conditions where Rh clusters and single atom mixtures were identified. We found that the PES of Pt and Rh adatoms are comparatively different. More sites are accessible to a Rh single-atom at low temperatures. Our simulations show that Rh can stabilize on a higher diversity of coordinatively distinct environments, occupying both the empty $Cu_xO$ ring and the $O_{adatom}$-occupied $Cu_xO$ ring. Within the same energy range, Pt can only favorably occupy the empty $Cu_xO$ ring, which reinforce the experimental observation that the coordination environment of Pt is relatively more homogeneous than Rh. The oxophilicity of the metal adatom plays a major role in enabling adatom migration across the "29" oxide. The higher oxophilicity of Rh facilitates low energy barriers to form new bonds with the oxide rings as the Rh

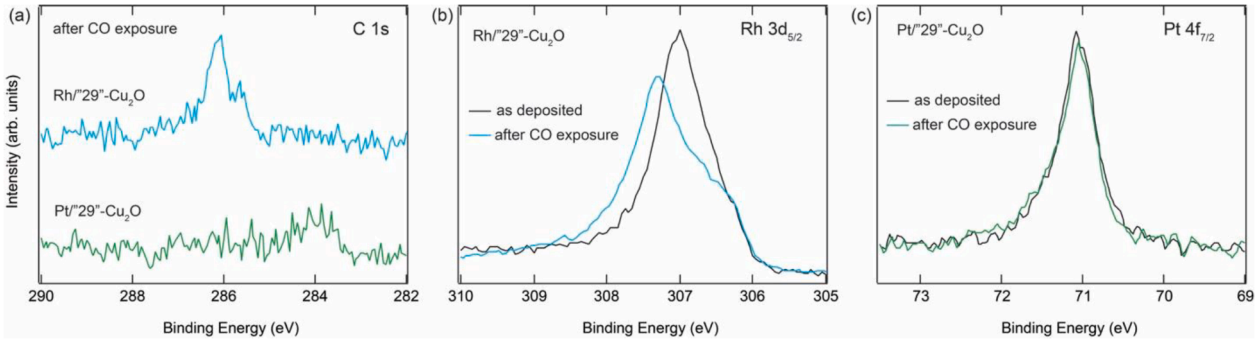


**Fig. 10.** (a) C 1*s* XPS spectra of "29" $Cu_2O$ with 1% Rh (top) and 1% Pt (bottom) after exposure to $1 \times 10^{-4}$ Torr of CO for 30 s at 300 K. (b) Rh $3d_{5/2}$ peak of 1% Rh deposited on "29" $Cu_2O$ before (black) and after (blue) CO exposure. (b) Pt $4f_{7/2}$ peak of 1% Pt deposited on "29" $Cu_2O$ before (black) and after (green) CO exposure.

moves along the path. We also found that the adsorption of Pt is more strongly governed by its bonding with Cu. This further makes it more difficult for Pt to cause defects on the oxide and migrate as compared to Rh.

We found that the difference in character between the Pt and Rh species directly affect their ability to bind to CO at the very low coverage of 1% ML. As Pt single-atoms do not interact with the oxide layer strong enough, defects seldom form on the "29" oxide, blocking its access to CO adsorbates. As Rh atoms are relatively more mobile and interact more strongly with the oxide layer, they retain better access to the CO adsorbates. We infer that the higher oxophilic character of Rh atoms is proportional to its ability to form defects on the "29" oxide, influencing its chemical activity with other adsorbates. Our work thus shows that the stabilizing factors of single-atoms on bulk oxides (i.e. strong interactions with surface O) can in fact become driving factors for mobility on transitional surfaces. Additionally, we highlight that the connection between defect formation and the single-atom sites can give fundamental insights about their accessibility and thus the nature of the active sites.

## Declaration of Competing Interest

The authors declare the following financial interests/personal relationships which may be considered as potential competing interests: E. Charles H. Sykes reports financial support was provided by US Department of Energy. Jean-Sabin McEwen reports financial support was provided by National Science Foundation.

## Data availability

Data will be made available on request.

## Acknowledgements

Financial support at Washington State University was provided by the National Science Foundation CAREER program under contract No. CBET-1653561. Financial support for the experimental work at Tufts University was provided by the US Department of Energy, BES, Catalysis Science program under contract No. DE-SC0021196. This work used the Extreme Science and Engineering Discovery Environment (XSEDE) [61], which is supported by National Science Foundation grant number ACI-1548562. Additional computer time for the computational work was performed using EMSL, a national scientific user facility sponsored by the Department of Energy's Office of Biological and Environmental Research and located at PNNL. PNNL is a multi-program national laboratory operated for the US DOE by Battelle. This research used resources of the 23-ID-2 (IOS) beamline of the National Synchrotron Light Source II, a U.S. Department of Energy (DOE) Office of Science User Facility operated for the DOE Office of Science by Brookhaven National Laboratory under Contract No. DE-SC0012704. We would also like to thank Phillip Christopher for fruitful discussions.

## Appendix A. Supplementary material

Supplementary data to this article can be found online at https://doi.org/10.1016/j.apsusc.2023.157145.

## References

[1] A.T. Bell, The Impact of Nanoscience on Heterogeneous Catalysis, Science 299 (5613) (2003) 1688–1691, https://doi.org/10.1126/science.1083671.
[2] R. Schlögl, Heterogeneous Catalysis, Angew. Chemie Int. Ed. 54 (2015) 3465–3520, https://doi.org/10.1002/anie.201410738.
[3] C.G. Freyschlag, R.J. Madix, Precious Metal Magic: Catalytic Wizardry, Mater. Today. 14 (2011) 134–142, https://doi.org/10.1016/S1369-7021(11)70085-2.
[4] B. Qiao, A. Wang, X. Yang, L.F. Allard, Z. Jiang, Y. Cui, J. Liu, J. Li, T. Zhang, Single-Atom Catalysis of CO Oxidation Using $Pt_1/FeO_x$, Nat. Chem. 3 (2011) 634–641, https://doi.org/10.1038/nchem.1095.
[5] X.-F. Yang, A. Wang, B. Qiao, J. Li, J. Liu, T. Zhang, Single-Atom Catalysts: A New Frontier in Heterogeneous Catalysis, Acc. Chem. Res. 46 (2013) 1740–1748, https://doi.org/10.1021/ar300361m.
[6] T.W. van Deelen, C. Hernández Mejía, K.P. de Jong, Control of Metal-Support Interactions in Heterogeneous Catalysts to Enhance Activity and Selectivity, Nat. Catal. 2 (2019) 955–970, https://doi.org/10.1038/s41929-019-0364-x.
[7] H.V. Thang, G. Pacchioni, L. DeRita, P. Christopher, Nature of Stable Single Atom Pt Catalysts Dispersed on Anatase $TiO_2$, J. Catal. 367 (2018) 104–114, https://doi.org/10.1016/j.jcat.2018.08.025.
[8] Y. Tang, C. Asokan, M. Xu, G.W. Graham, X. Pan, P. Christopher, J. Li, P. Sautet, Rh Single Atoms on $TiO_2$ Dynamically Respond to Reaction Conditions by Adapting their Site, Nat. Commun. 10 (2019) 1–10, https://doi.org/10.1038/s41467-019-12461-6.
[9] L. DeRita, S. Dai, K. Lopez-Zepeda, N. Pham, G.W. Graham, X. Pan, P. Christopher, Catalyst Architecture for Stable Single Atom Dispersion Enables Site-Specific Spectroscopic and Reactivity Measurements of CO Adsorbed to Pt Atoms, Oxidized Pt Clusters, and Metallic Pt Clusters on $TiO_2$, J. Am. Chem. Soc. 139 (2017) 14150–14165, https://doi.org/10.1021/jacs.7b07093.
[10] J. Liu, A.J.R. Hensley, G. Giannakakis, A.J. Therrien, A. Sukkar, A.C. Schilling, K. Groden, N. Ulumuddin, R.T. Hannagan, M. Ouyang, M. Flytzani-Stephanopoulos, J.-S. McEwen, E.C.H. Sykes, Developing Single-Site Pt Catalysts for the Preferential Oxidation of CO: A Surface Science and First Principles-Guided Approach, Appl. Catal. B Environ. 284 (2021), 119716, https://doi.org/10.1016/j.apcatb.2020.119716.
[11] D.T.T. US, Advanced Combustion and Emission Control Technical Team Roadmap, 2018. http://www1.eere.energy.gov/vehiclesandfuels/pdfs/program/acec_roadmap_june2013.pdf.
[12] B. Han, T. Li, J. Zhang, C. Zeng, H. Matsumoto, Y. Su, B. Qiao, T. Zhang, A Highly Active $Rh_1/CeO_2$ Single-Atom Catalyst for Low-Temperature CO Oxidation, Chem. Commun. 56 (2020) 4870–4873, https://doi.org/10.1039/d0cc00230e.
[13] B. Han, R. Lang, H. Tang, J. Xu, X.K. Gu, B. Qiao, J. Liu, Superior Activity of $Rh_1$/ZnO Single-Atom Catalyst for CO Oxidation, Chinese, J. Catal. 40 (2019) 1847–1853, https://doi.org/10.1016/S1872-2067(19)63411-X.
[14] B. Qiao, J.X. Liang, A. Wang, C.Q. Xu, J. Li, T. Zhang, J.J. Liu, Ultrastable Single-Atom Gold Catalysts with Strong Covalent Metal-Support Interaction (CMSI), Nano Res. 8 (2015) 2913–2924, https://doi.org/10.1007/s12274-015-0796-9.
[15] J. Guzman, B.C. Gates, Structure and Reactivity of a Mononuclear Gold-Complex Catalyst Supported on Magnesium Oxide, Angew. Chemie Int. Ed. 42 (2003) 690–693, https://doi.org/10.1002/anie.200390191.
[16] Z. Jakub, J. Hulva, P.T.P. Ryan, D.A. Duncan, D.J. Payne, R. Bliem, M. Ulreich, P. Hofegger, F. Kraushofer, M. Meier, M. Schmid, U. Diebold, G.S. Parkinson, Adsorbate-Induced Structural Evolution Changes the Mechanism of CO Oxidation on a $Rh/Fe_3O_4$(001) Model Catalyst, Nanoscale. 12 (2020) 5866–5875, https://doi.org/10.1039/c9nr10087c.
[17] Q.i. Fu, H. Saltsburg, M. Flytzani-Stephanopoulos, Active Nonmetallic Au and Pt Species on Ceria-Based Water-Gas Shift Catalysts, Science 301 (5635) (2003) 935–938, https://doi.org/10.1126/science.1085721.
[18] R. Bliem, J. van der Hoeven, A. Zavodny, O. Gamba, J. Pavelec, P.E. de Jongh, M. Schmid, U. Diebold, G.S. Parkinson, An Atomic-Scale View of CO and $H_2$ Oxidation on a $Pt/Fe_3O_4$ Model Catalyst, Angew. Chemie Int. Ed. 54 (2015) 13999–14002, https://doi.org/10.1002/anie.201507368.
[19] K. Liu, R. Qin, L. Zhou, P. Liu, Q. Zhang, W. Jing, P. Ruan, L. Gu, G. Fu, N. Zheng, $Cu_2O$-Supported Atomically Dispersed Pd Catalysts for Semihydrogenation of Terminal Alkynes: Critical Role of Oxide Supports, CCS Chem. 1 (2019) 207–214, https://doi.org/10.31635/ccschem.019.20190008.
[20] A.J. Therrien, A.J.R.R. Hensley, M.D. Marcinkowski, R. Zhang, F.R. Lucci, B. Coughlin, A.C. Schilling, J.S. McEwen, E.C.H. Sykes, An Atomic-Scale View of Single-Site Pt Catalysis for Low-Temperature CO Oxidation, Nat. Catal. 1 (2018) 192–198, https://doi.org/10.1038/s41929-018-0028-2.
[21] S.A. Jagtap, M.A. Bhosale, T. Sasaki, B.M. Bhanage, $Rh/Cu_2O$ Nanoparticles: Synthesis, Characterization and Catalytic Application as a Heterogeneous Catalyst in Hydroformylation Reaction, Polyhedron. 120 (2016) 162–168, https://doi.org/10.1016/j.poly.2016.08.026.
[22] J. Liu, Aberration-Corrected Scanning Transmission Electron Microscopy in Single-Atom Catalysis: Probing the Catalytically Active Centers, Chinese, J. Catal. 38 (2017) 1460–1472, https://doi.org/10.1016/S1872-2067(17)62900-0.
[23] G.S. Parkinson, Single-Atom Catalysis: How Structure Influences Catalytic Performance, Catal. Letters. 149 (2019) 1137–1146, https://doi.org/10.1007/s10562-019-02709-7.
[24] C.T. Campbell, Transition Metal Oxides: Extra Thermodynamic Stability as Thin Films, Phys. Rev. Lett. 96 (2006) 23–26, https://doi.org/10.1103/PhysRevLett.96.066106.
[25] J. Liang, Q. Yu, X. Yang, T. Zhang, J. Li, A Systematic Theoretical Study on $FeO_x$-Supported Single-Atom Catalysts: $M_1/FeO_x$ for CO Oxidation, Nano Res. 11 (2018) 1599–1611, https://doi.org/10.1007/s12274-017-1775-0.
[26] T. Risse, S. Shaikhutdinov, N. Nilius, M. Sterrer, H.J. Freund, Gold Supported on Thin Oxide Films: From Single Atoms to Nanoparticles, Acc. Chem. Res. 41 (2008) 949–956, https://doi.org/10.1021/ar800078m.
[27] Y.G. Wang, D. Mei, V.A. Glezakou, J. Li, R. Rousseau, Dynamic Formation of Single-Atom Catalytic Active Sites on Ceria-Supported Gold Nanoparticles, Nat. Commun. 6 (2015) 1–8, https://doi.org/10.1038/ncomms7511.
[28] A.J. Therrien, R. Zhang, F.R. Lucci, M.D. Marcinkowski, A. Hensley, J.-S. McEwen, E.C.H. Sykes, Structurally Accurate Model for the "29"-Structure of $Cu_xO/Cu(111)$: A DFT and STM Study, J. Phys. Chem. C. 120 (2016) 10879–10886, https://doi.org/10.1021/acs.jpcc.6b01284.

[29] A.A. Ogwu, T.H. Darma, E. Bouquerel, Electrical Resistivity of Copper Oxide Thin Films Prepared by Reactive Magnetron Sputtering, J. Achiev. Mater. Manuf. Eng. 24 (2007) 172–177.
[30] V.R. Cooper, A.M. Kolpak, Y. Yourdshahyan, A.M. Rappe, Oxide-Supported Metal Thin-Film Catalysts: The How and Why, in, Nanotechnol. Catal. (2007) 13–21, https://doi.org/10.1007/978-0-387-34688-5_2.
[31] X. Shao, S. Prada, L. Giordano, G. Pacchioni, N. Nilius, H.J. Freund, Tailoring the Shape of Metal Ad-Particles by Doping the Oxide Support, Angew. Chemie - Int. Ed. 50 (2011) 11525–11527, https://doi.org/10.1002/anie.201105355.
[32] K.N. Woods, T.-H. Chiang, P.N. Plassmeyer, M.G. Kast, A.C. Lygo, A.K. Grealish, S. W. Boettcher, C.J. Page, High-κ Lanthanum Zirconium Oxide Thin Film Dielectrics from Aqueous Solution Precursors, ACS Appl. Mater. Interfaces. 9 (2017) 10897–10903, https://doi.org/10.1021/acsami.7b00915.
[33] T. Narushima, H. Tsukamoto, T. Yonezawa, High Temperature Oxidation Event of Gelatin Nanoskin-Coated Copper Fine Particles Observed by In Situ TEM, AIP Adv. 2 (4) (2012), 042113, https://doi.org/10.1063/1.4759498.
[34] A.J.R. Hensley, A.J. Therrien, R. Zhang, M.D. Marcinkowski, F.R. Lucci, E.C. H. Sykes, J.-S. McEwen, CO Adsorption on the " 29 " CuO/Cu(111) Surface : An Integrated DFT, STM, and TPD Study, J. Phys. Chem. C. 120 (2016) 25387–25394, https://doi.org/10.1021/acs.jpcc.6b07670.
[35] A.J. Therrien, A.J.R. Hensley, R. Zhang, A. Pronschinske, M.D. Marcinkowski, J.-S. McEwen, E.C.H. Sykes, Characterizing the Geometric and Electronic Structure of Defects in the "29" Copper Surface Oxide, J. Chem. Phys. 147 (22) (2017) 224706, https://doi.org/10.1063/1.4996729.
[36] A.J. Therrien, K. Groden, A.J.R. Hensley, A.C. Schilling, R.T. Hannagan, M. D. Marcinkowski, A. Pronschinske, F.R. Lucci, E.C.H. Sykes, J.S. McEwen, Water Activation by Single Pt Atoms Supported on a $Cu_2O$ Thin Film, J. Catal. 364 (2018) 166–173, https://doi.org/10.1016/j.jcat.2018.04.024.
[37] G. Kresse, J. Furthmüller, Efficient Iterative Schemes for Ab Initio Total-Energy Calculations Using a Plane-Wave Basis Set, Phys. Rev. B. 54 (1996) 11169–11186, https://doi.org/10.1103/PhysRevB.54.11169.
[38] G. Kresse, J. Hafner, Ab Initio Molecular Dynamics for Liquid Metals, Phys. Rev. B. 47 (1) (1993) 558–561, https://doi.org/10.1103/PhysRevB.47.558.
[39] K. Lejaeghere, G. Bihlmayer, T. Björkman, P. Blaha, S. Blügel, V. Blum, D. Caliste, I. E. Castelli, S.J. Clark, A. Dal Corso, S. de Gironcoli, T. Deutsch, J.K. Dewhurst, I. Di Marco, C. Draxl, M. Dułak, O. Eriksson, J.A. Flores-Livas, K.F. Garrity, L. Genovese, P. Giannozzi, M. Giantomassi, S. Goedecker, X. Gonze, O. Grånäs, E.K.U. Gross, A. Gulans, F. Gygi, D.R. Hamann, P.J. Hasnip, N.A.W. Holzwarth, D. Iuşan, D. B. Jochym, F. Jollet, D. Jones, G. Kresse, K. Koepernik, E. Küçükbenli, Y. O. Kvashnin, I.L.M. Locht, S. Lubeck, M. Marsman, N. Marzari, U. Nitzsche, L. Nordström, T. Ozaki, L. Paulatto, C.J. Pickard, W. Poelmans, M.I.J. Probert, K. Refson, M. Richter, G.-M. Rignanese, S. Saha, M. Scheffler, M. Schlipf, K. Schwarz, S. Sharma, F. Tavazza, P. Thunström, A. Tkatchenko, M. Torrent, D. Vanderbilt, M.J. van Setten, V. Van Speybroeck, J.M. Wills, J.R. Yates, G.-X. Zhang, S. Cottenier, Reproducibility in density functional theory calculations of solids, Science 351 (6280) (2016), https://doi.org/10.1126/science.aad3000.
[40] G. Kresse, D. Joubert, From Ultrasoft Pseudopotentials to the Projector Augmented-Wave Method, Phys. Rev. B - Condens. Matter Mater. Phys. 59 (1999) 11–19, https://doi.org/10.1103/PhysRevB.59.1758.
[41] J.P. Perdew, K. Burke, M. Ernzerhof, Generalized Gradient Approximation Made Simple, Phys. Rev. Lett. 77 (1996) 3865–3868, https://doi.org/10.1103/PhysRevLett.77.3865.
[42] P.J. Feibelman, Surface-Diffusion Mechanism Versus Electric Field: Pt/Pt(001), Phys. Rev. B - Condens. Matter Mater. Phys. 64 (2001) 1–6, https://doi.org/10.1103/PhysRevB.64.125403.
[43] H.J. Monkhorst, J.D. Pack, Special points for Brillouin-zone integrations, Phys. Rev. B. 13 (1976) 5188–5192, https://doi.org/10.1103/PhysRevB.13.5188.
[44] K.B. Wiberg, P.R. Rablen, Comparison of Atomic Charges Derived via Different Procedures, J. Comput. Chem. 14 (1993) 1504–1518, https://doi.org/10.1002/jcc.540141213.
[45] G. Henkelman, A. Arnaldsson, H. Jónsson, A Fast and Robust Algorithm for Bader Decomposition of Charge Density, Comput. Mater. Sci. 36 (2006) 354–360, https://doi.org/10.1016/j.commatsci.2005.04.010.
[46] S. Nagase, K. Morokuma, An ab initio Molecular Orbital Study of Organic Reactions. The Energy, Charge, and Spin Decomposition Analyses at the Transition State and Along the Reaction Pathway, J. Am. Chem. Soc. 100 (1978) 1666–1672, https://doi.org/10.1021/ja00474a005.
[47] F.M. Bickelhaupt, K.N. Houk, Analyzing Reaction Rates with the Distortion/Interaction-Activation Strain Model, Angew. Chemie - Int. Ed. 56 (2017) 10070–10086, https://doi.org/10.1002/anie.201701486.
[48] L.P. Wolters, F.M. Bickelhaupt, The Activation Strain Model and Molecular Orbital Theory, Wiley Interdiscip. Rev. Comput. Mol. Sci. 5 (2015) 324–343, https://doi.org/10.1002/wcms.1221.
[49] G. Henkelman, H. Jónsson, Improved Tangent Estimate in the Nudged Elastic Band Method for Finding Minimum Energy Paths and Saddle Points, J. Chem. Phys. 113 (2000) 9978–9985, https://doi.org/10.1063/1.1323224.
[50] G. Henkelman, B.P. Uberuaga, H. Jónsson, A Climbing Image Nudged Elastic Band Method for Finding Saddle Points and Minimum Energy Paths, J. Chem. Phys. 113 (2000) 9901–9904, https://doi.org/10.1063/1.1329672.
[51] G. Henkelman, H. Jónsson, A Dimer Method for Finding Saddle Points on High Dimensional Potential Surfaces Using Only First Derivatives, J. Chem. Phys. 111 (1999) 7010–7022, https://doi.org/10.1063/1.480097.
[52] D. Sheppard, R. Terrell, G. Henkelman, Optimization Methods for Finding Minimum Energy Paths, J. Chem. Phys. 128 (2008) 1–10, https://doi.org/10.1063/1.2841941.
[53] A.C. Schilling, N. Ulumuddin, V. Çinar, R.T. Hannagan, K. Groden, Y. Wang, L. A. Cramer, P.L. Kress, D.A. Patel, B. Vo, A. Hunt, P. Christopher, I. Waluyo, J.-S. McEwen, E.C.H. Sykes, Elucidating CO Oxidation Pathways on Rh Atoms and Clusters on the "29" $Cu_2O$/Cu(111) Surface, J. Phys. Chem. C. 126 (2022) 11091–11102, https://doi.org/10.1021/acs.jpcc.2c02699.
[54] R.D. Shannon, Synthesis and Properties of Two New Members of the Rutile Family $RhO_2$ and $PtO_2$, Solid State Commun. 6 (1968) 139–143, https://doi.org/10.1016/0038-1098(68)90019-7.
[55] G.S. Parkinson, Z. Novotny, G. Argentero, M. Schmid, J. Pavelec, R. Kosak, P. Blaha, U. Diebold, Carbon Monoxide-Induced Adatom Sintering in a Pd-$Fe_3O_4$ Model Catalyst, Nat. Mater. 12 (2013) 724–728, https://doi.org/10.1038/nmat3667.
[56] G. Collinge, Y. Xiang, R. Barbosa, J.-S. McEwen, N. Kruse, CO-Induced Inversion of the Layer Sequence of a Model CoCu Catalyst, Surf. Sci. 648 (2016) 74–83, https://doi.org/10.1016/j.susc.2015.10.014.
[57] F. Jensen, F. Besenbacher, I. Stensgaard, Two New Oxygen Induced Reconstructions on Cu(111), Surf. Sci. 269–270 (1992) 400–404, https://doi.org/10.1016/0039-6028(92)91282-G.
[58] G. Blyholder, Molecular Orbital View of Chemisorbed Carbon Monoxide, J. Phys. Chem. 68 (1964) 2772–2778, https://doi.org/10.1021/j100792a006.
[59] F. Garcia-Martinez, F. Schiller, S. Blomberg, M. Shipilin, L.R. Merte, J. Gustafson, E. Lundgren, J.E. Ortega, CO Chemisorption on Vicinal Rh(111) Surfaces Studied with a Curved Crystal, J. Phys. Chem. C. 124 (2020) 9305–9313, https://doi.org/10.1021/acs.jpcc.0c00039.
[60] A.C. Schilling, K. Groden, J.P. Simonovis, A. Hunt, R.T. Hannagan, V. Çlnar, J.-S. McEwen, E.C.H. Sykes, I. Waluyo, Accelerated $Cu_2O$ Reduction by Single Pt Atoms at the Metal-Oxide Interface, ACS Catal. 10 (2020) 4215–4226, https://doi.org/10.1021/acscatal.9b05270.
[61] N.W.-D.J. Towns, T. Cockerill, M. Dahan, I. Foster, K. Gaither, A. Grimshaw, V. Hazlewood, S. Lathrop, D. Lifka, G.D. Peterson, R. Roskies, J.R. Scott, N. Wilkins-Diehr, J. Towns, T. Cockerill, M. Dahan, I. Foster, K. Gaither, A. Grimshaw, V. Hazlewood, S. La, XSEDE: Accelerating Scientific Discovery, Comput. Sci. Eng. 16 (2014) 62–74, https://doi.org/10.1109/MCSE.2014.80.